Composite Structures 376 (2026) 119796

Contents lists available at ScienceDirect

Composite Structures

journal homepage: www.elsevier.com/locate/compstruct

Simultaneous optimization of composite shells, metallic components and their joints☆

Konrad Schneider *, Olaf Ambrozkiewicz, Benedikt Kriegesmann

Structural mechanics in lightweight design, Hamburg University of Technology, Germany

ARTICLE INFO

Keywords:
Topology optimization
Strength constraints
Assembly optimization
Joint optimization

ABSTRACT

This paper presents an approach for the simultaneous topology optimization of an isotropic (e.g. metallic) component, the layup optimization of a composite part and the search for the optimized position of joints between the parts. Within a gradient-based optimization, a failure criterion for the composite acts as a constraint. The constraint's gradients with respect to fiber orientations, pseudo densities of the isotropic elements, and joint positions are presented. As a demonstrative example, the load introduction into an isotropic component attached to a composite plate is analyzed. The results reveal a significant influence of the considered constraint on the optimized overall design.

1. Introduction

Composite components have successfully been applied for large lightweight structures. However, they are mostly used for thin-walled structures, such as fuselage or wings panels. Nevertheless, in areas where loads are introduced and complex three-dimensional stress states are present, metallic structures are still the first choice (see, e.g. [1]). In order to maintain the focus on lightweight design, the advances in the field of additive manufacturing allow for tailoring such metallic structures to be as lightweight as possible, while withstanding the occurring stress states. One example for such a load introduction element, which is manufactured by additive manufacturing, is the flight crew rest compartment (FCRC) bracket of the Airbus A350, which became famous as being the first flying additively manufactured part (see, e.g. [2–4]). However, by increasing the stiffness of a load introduction element, e.g. a bracket, stress concentrations in the base structure may occur. Especially from a lightweight construction point of view, the base structure might also be subject to a weight and stiffness optimization process itself and therefore more vulnerable to stress peaks and non-homogeneous force transmissions. It is therefore logical to consider the strength of the bracket, the base structure, and any required fasteners in the design and optimization process by means of a holistic approach. Questions of an altered topological shape of the load introducing element, an optimized joint pattern or structural changes of the fastening structure compared to the individual component analysis may arise. An optimization process considering an entire assembly, consisting of a mixture of isotropic and fiber-reinforced components, could lead to a significantly improved overall design. To the authors' knowledge, such an optimization has not been done before. This aspect therefore represents the core contribution of the present work and extends our previous endeavors [5] on assembled isotropic parts without strength constraints. There, a simultaneous optimization of the topology and the joint positions results in an improved assembly design. In the current work, we are extending this idea by including the strength and structural properties of the base component, i.e. the fiber-reinforced panel, in a simultaneous optimization via additional strength constraints and the augmentation of the design variables by fiber orientation angles. The simultaneous optimization of topology and fiber orientation is an active field of research, e.g. motivated by the advances in 3D printing of endless fiber reinforced components (see, for instance, [6–8]). It needs to be emphasized, however, that the current contribution is not located in this field. The part that is subject to topology optimization is always an isotropic part which in turn is connected to a composite plate. The focus of this paper is the interaction of both components and the influence of the presence of the composite part on the topology of the optimized isotropic component.

In the following section, we introduce the example that is examined throughout the paper. In Section 3, the optimization formulation and setup are given. Section 4 describes the gradient calculation. In the results Section 5, we show how considering the strength of the composite part affects the bracket design for different connection types.

☆ This article is part of a Special issue entitled: 'Rolfes 65th' published in Composite Structures.

* Corresponding author.
E-mail address: konrad.schneider@tuhh.de (K. Schneider).

https://doi.org/10.1016/j.compstruct.2025.119796
Received 26 June 2025; Received in revised form 12 September 2025; Accepted 23 October 2025
Available online 3 November 2025

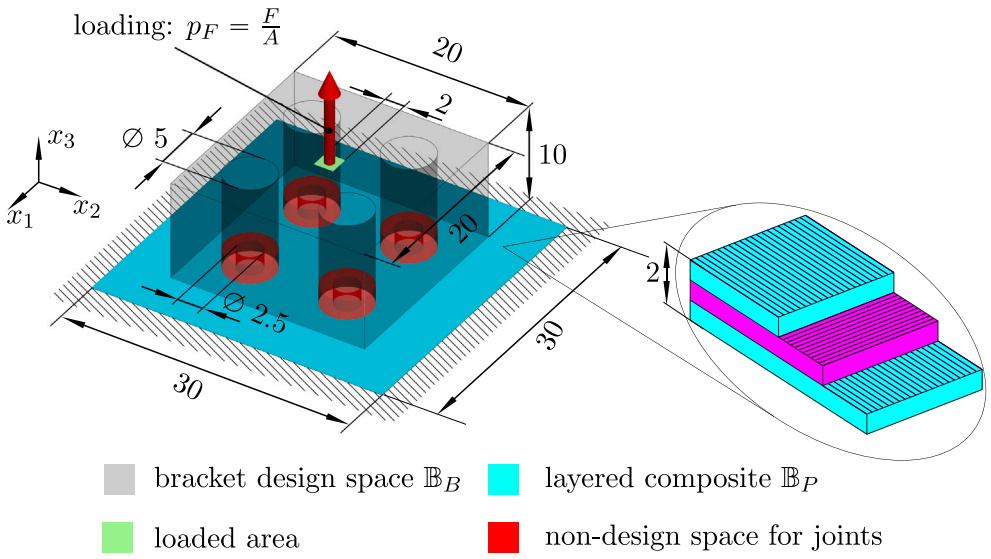

Fig. 1. Initial model setup of the bracket on a panel example for the case of four joints connecting both components in generic length units.

2. Example considered

Fig. 1 depicts the studied bracket on a plate example (see [5]) using gernerig length units. The bracket design space $\mathbb{B}_B$ is loaded by a pressure p_F acting on a quadratic surface area A, which results in a net force F. The panel, denoted by $\mathbb{B}_P$, is fully clamped at the sides. The mounting between the bracket and the panel can be twofold: The bracket's design space is either connected to the panel over the entire surface, e.g. glued together, or attached to the panel via four joints, which requires some additional modeling effort. The panel itself is a composite laminate which consists of three unidirectional carbon fiber reinforced (CFR) plies. Typically, composite laminates consist of many more plies. Quasi-isotropic laminates, which are often used in industry, do not allow to investigate and demonstrate the influence of the interaction of bracket optimization and composite parts. To capture and isolate the dominating effects on the assembly optimization, we restrict the model to only three layers, which at the same time represent extreme cases. The subsequent anisotropic deformation and strength behavior of the panel due to the laminates has a direct influence on the optimal topology of the bracket.

In the case where joints like rivets or bolts connect the two components, the regions above the joints must be free of any obstacles to accommodate an unobstructed assembly process. Therefore, a void non-design space is introduced in a cylindrical space above the joints in the bracket's design space. Additionally, force transfer zones around the connections must also be present to provide e.g. a bolt head support. These regions have to be solid non-design spaces and are shown in red in Fig. 1. Bolt insertion is only possible if adequate drill holes are present. These drill holes concern the bracket and panel regions and are again modeled as empty non-design spaces. Whenever these types of joints are used in the optimization, they are considered movable instances for which the final location is also part of the optimization problem. The associated non-design spaces will always move together with the joints.

The considered material behavior is modeled as linear elastic under small deformations, resulting in a linear deformation analysis. For a realistic setting, the bracket material and the bolt material are assumed to be titanium with the isotropic elastic parameters E_{Ti} and ν_{Ti}, see [9]. A laminate ply of the CFR panel is characterized by its transversal isotropic linear elastic material behavior. The fiber direction is denoted by the fiber angle φ in the x_1–x_2-plane. If the uniaxial fiber orientation is parallel to the x_1-direction ($\varphi = 0$) the elastic material parameters are given by E_1, E_2, G_{12} and ν_{12}, see [10]. Table 1 lists the used parameters. These parameters define an elasticity tensor $\mathbb{C}$ which depends on the orientation angle φ in case of the CFR plies. This angle determines the rotation between the local x–y-plane and the x_1–x_2-plane of the global coordinate system. To assess the strength of the CFR panel, we utilize the popular Tsai–Wu failure criterion [11] for every ply, that is

$$TW(\underline{\sigma}_L) = \underline{\sigma}_L^T \underline{F} + \underline{\sigma}_L^T \underline{\underline{F}} \underline{\sigma}_L^T \leq 1 \tag{1}$$

with the parameter vector $\underline{F}$ and symmetric parameter matrix $\underline{\underline{F}}$. The stress tensor of the panel is denoted in the local ply coordinate system as

$$\underline{\sigma}_L = \begin{bmatrix} \sigma_{11} & \sigma_{22} & \sigma_{12} \end{bmatrix}^T \tag{2}$$

in Voigt notation, which is utilized throughout this work. For a plane stress state, as it is assumed for the panel, the non-vanishing strength parameters are typically given by the following relations:

$$\begin{aligned} F_1 &= \frac{1}{\sigma_{1t}} - \frac{1}{\sigma_{1c}}\,, \quad F_{11} = \frac{1}{\sigma_{1c}\sigma_{1t}} \\ F_2 &= \frac{1}{\sigma_{2t}} - \frac{1}{\sigma_{2c}}\,, \quad F_{22} = \frac{1}{\sigma_{2c}\sigma_{2t}}\,. \\ F_{44} &= \frac{1}{\tau_{12}^2}\,, \quad F_{12} = -\frac{1}{2}\sqrt{F_{11}F_{22}} \end{aligned} \tag{3}$$

Here, σ_{1t}, σ_{1c} and σ_{2t}, σ_{2c} are the strength values for a single ply under uniaxial loading in x_1 or x_2 direction for tension or compression, respectively. τ_{12} is the failure shear stress in a pure shear test. The coupling term F_{12} is heuristically chosen to fulfill the stability condition emanating from a biaxial loading, see [11]. In this setting, the strength parameters can be determined experimentally, see [10].

In the case of a bolted connection between the bracket and panel, the bolts also have a certain stiffness k_{Bolt}, which is given by

$$k_{Bolt} = \frac{E_{Ti} A_{Bolt}}{t_{Clamp}} \tag{4}$$

with A_{Bolt} being the cross-sectional area of the bolts and t_{Clamp} being the clamping length.

The deformation simulation is done by means of a finite element analysis, where the bracket is discretized by a regular mesh of 256 000 cuboidal bilinear hexahedral elements of size $[0.25 \times 0.25 \times 0.25]$. In the bracket domain $\mathbb{B}_B$, all nodes possess 3 translational degrees of freedom. The panel is discretized by a regular mesh of 14 400 quadratic shell elements of size $[0.25 \times 0.25]$. For the shell element formulation, we adopted the MITC4 element formulation, see [12,13]. In the panel

Table 1
Linear elastic and strength parameters of the bracket and panel, taken from [9] and [10].

Titanium bracket		CFR ply (elastic)		CFR ply (strength)		Bolts	
E_{Ti}	163,000 MPa	E_x	171,420 MPa	σ_{1t}	2,326 MPa	k_{Bolt}	$4 \cdot 10^5$ N/mm
ν_{Ti}	0.34	E_y	9,080 MPa	σ_{1c}	1,200 MPa		
		G_{xy}	5,290 MPa	σ_{2t}	62 MPa		
		ν_{xy}	0.32	σ_{2c}	200 MPa		
				τ_{12}	92 MPa		

domain $\mathbb{B}_P$, all nodes possess 3 translational and 3 rotational degrees of freedom. This discretization leads to the global linear system

$$\underline{\underline{K}}\,\underline{u} = \underline{F}$$

$$\begin{bmatrix} \underline{\underline{K}}_B & \underline{\underline{0}} & \underline{\underline{0}} & \begin{bmatrix} \underline{\underline{G}}^T \end{bmatrix} \\ \underline{\underline{0}} & \underline{\underline{K}}_P & \underline{\underline{0}} & \\ \underline{\underline{0}} & \underline{\underline{0}} & \underline{\underline{K}}_J & \\ \begin{bmatrix} \underline{\underline{G}} \end{bmatrix} & & & \underline{\underline{0}} \end{bmatrix} \begin{bmatrix} \underline{u}_B \\ \underline{u}_P \\ \underline{u}_J \\ \underline{\lambda} \end{bmatrix} = \begin{bmatrix} \underline{F}_B \\ \underline{F}_P \\ \underline{F}_J \\ \underline{b} \end{bmatrix}, \tag{5}$$

which can be divided into the bracket region degree of freedom indexed with $(\dots)_B$, panel degree of freedom indexed by $(\dots)_P$, and joint degree of freedom $(\dots)_J$. $\underline{\lambda}$ denotes the vector holding the Lagrange-Multipliers that enforce possible coupling constraints, $\underline{\underline{G}}$ is the constraint matrix and $\underline{b}$ a possible right-hand-side of non-homogeneous constraints. The coupling between the bracket and the panel is twofold, depending on the problem considered. If no joints are considered, the translational degrees of freedom of coinciding nodes of the bracket and panel are directly coupled. If joints are considered the method suggested in [5] is employed. The constraint matrix $\underline{\underline{G}}$ varies in shape and value, depending on the coupling case.

3. Design optimization setup

Since this work is based on [5], we briefly summarize the general optimization setting.

3.1. Single part compliance topology optimization

The basis of the entire topology optimization process is the compliance optimization problem that is given by

$$\begin{aligned} \min_{\varrho_e} c \quad s.t. \quad & \underline{\underline{K}}\,\underline{u} - \underline{F} = \underline{0} \\ & 0 \le \varrho_e \le 1 \\ & \frac{\sum_e v_e}{V_0} - v_f \le 0 \end{aligned} \qquad \forall\, e \in \mathbb{B}_B \ . \tag{6}$$

The compliance objective function $c = \underline{u}_B^T \underline{F}_B$ depends on the global deformation and force vector parts $\underline{u}_B$ and $\underline{F}_B$ of the discretized bracket.[1] The design variables are limited by box constraints, and a volume constraint is applied to the bracket, where v_e is the volume of each element, V_0 is the total design space volume, and the volume fraction is $v_f = 15\%$.

The design variables are the pseudo densities ϱ_e of every finite element of the bracket region $\mathbb{B}_B$. These pseudo densities are filtered using

$$\tilde{\varrho}_e = \frac{\sum_j w(\underline{c}^j - \underline{c}^e) v_j \varrho_j}{\sum_j w(\underline{c}^j - \underline{c}^e) v_j} \quad \text{with} \quad w(\underline{x}) = \max(r - \|\underline{x}\|_2, 0) \quad \text{and} \quad r = 0.75 \tag{7}$$

with the element centers $\underline{c}^e$, the element volumes v_j and the conic weighting function w that incorporates the filter radius r into this process. Filtering is applied to avoid checkerboarding and mesh-dependency of the result. Therefore, r is chosen to be three times the element edge length.

[1] The formulation used of the compliance is only possible for homogeneous Dirichlet-boundary conditions, which applies to the fully clamped panel. More general settings are discussed by e.g. Montemurro [14].

In the next step, the filtered densities are projected via

$$\bar{\varrho}_e = \frac{\tanh(\beta\eta) + \tanh(\beta[\tilde{\varrho}_e - \eta])}{\tanh(\beta\eta) + \tanh(\beta[1 - \eta])} \quad \text{for} \quad \eta = 0.5 \ , \ \beta \in \{1, 2, 4, 8\} \tag{8}$$

to sharpen the transitions from void to solid regions, i.e. to prevent unwanted intermediate regions and minimize spurious boundary effects. The sharpening parameter β is successively increased during the optimization process to improve convergence.

The Solid Isotropic Material with Penalization (SIMP) scheme is applied to the projected density field, see [15]. Therein, the effective Young's modulus E_e of each element e is interpolated via

$$E_e = E_{min} + [E_0 - E_{min}]\bar{\varrho}_e^p \quad \text{with} \quad E_{min} = 10^{-9} E_0 \tag{9}$$

with the penalization parameter $p = 4$ and the Young's modulus E_0 of the unpenalized material.

3.2. Surface connection between bracket and panel with strength constraints

In the case of a surface connection between the bracket and the panel, we equalize the translational degrees of freedom of the hexahedral elements of the bracket region and the shell elements of the panel region for coinciding nodes in the contact area and thus model the connection as perfectly bonded. Due to the congruent meshes, this coupling is straightforward, leading to a total size of the discretized system (5) of 875 166 degrees of freedom. To incorporate the strength condition for the panel (1), we augment the problem (6) by an additional inequality constraint namely the Tsai–Wu criterion, which depends quadratically on the stress. Typically, a scaling factor denoted as reserve factor RF is introduced to transform the strength condition into an inequality of the form $TW(RF\underline{\sigma}) \le 1$. The goal is to ensure $RF \ge 1$ in the whole panel domain. However, the use of the reserve factor RF might lead to numerical singularities, since a vanishing stress results in an infinite reserve factor. Therefore, the inverse of RF, namely the load factor LF, is used in the strength constraint, which eventually can be written as (see also Appendix A.1):

$$g_{LF}(LF) = LF - 1 = \frac{1}{RF(\underline{\sigma})} - 1 \le 0 \ . \tag{10}$$

In order to limit the number of constraints, only the maximum load factor of all the shell elements of the panel region is considered in the optimization constraint. The optimization problem then becomes:

$$\begin{aligned} \min_{\varrho_e} c \quad s.t. \quad & \underline{\underline{K}}\,\underline{u} - \underline{F} = \underline{0} \\ & 0 \le \varrho_e \le 1 \\ & \frac{\sum_e v_e}{V_0} - v_f \le 0 \\ & \max(LF_p) - 1 \le 0 \end{aligned} \qquad \forall\, e \in \mathbb{B}_B \ \text{ and } \ \forall\, p \in \mathbb{B}_P \ . \tag{11}$$

3.3. Discrete joint-based connection between bracket and panel with strength constraints

In the case of a discrete connection, the joints can be thought of as bolted connections with a certain bolt stiffness. Every joint i is described by its position $\underline{x}_i$ and the dimensions of the associated void and solid non-design space. The joints stay in contact with the surfaces of the parts at all times. The force transfer between bracket and panel is modeled with a ring pattern (red regions in Fig. 1). Inside this pattern, many spring elements are introduced in a regular fashion. One endpoint

of every spring element is connected to the surface of the bracket region and the other to the surface of the panel region. The springs' nodes are coupled to the respective parts through the shape functions of the parts' elements at the connection surface. The total stiffness of all springs in a single joint yields the desired total bolt stiffness. For the topology optimization, the material distribution is altered, since for every joint its associated non-design spaces are enforced in the density field (empty non-design regions and red solid regions in the design spaces of Fig. 1). Due to this modification, the projected densities used in Eq. (9) become the modified densities:

$$\bar{\varrho}_e \overset{\text{Modification}}{\rightarrow} \hat{\varrho}_e(\bar{\varrho}_e, \underline{x}_i) \,. \tag{12}$$

For more details on how to incorporate the non-design spaces associated with the joints into the density field of the topology optimization we refer the reader to [5].

To consider discrete joints, the design variables of problem (6) are augmented by the joint positions $\underline{x}_i$ for n_J joints, which leads to

$$\begin{aligned} \min_{\varrho_e, \underline{x}_i} \; & c \quad s.t. \quad \underline{\underline{\tilde{K}}}\,\underline{\tilde{u}} - \underline{\tilde{F}} = \underline{0} \\ & 0 \le \varrho_e \le 1 \\ & \underline{x}_{min} \le \underline{x}_i \le \underline{x}_{max} \\ & \frac{\sum_e v_e}{V_0} - v_f \le 0 \\ & \min_{i \neq j} d_{ij} - d_0 \le 0 \end{aligned} \qquad \forall\, e \in \mathbb{B}_B \text{ and } \forall i, j = \{1\,,\,\dots\,,\,n_J\}\,. \tag{13}$$

To account for manufacturing constraints, force transition regions and non-overlapping joints, the joint positions are constrained using the mutual joint distance $d_{ij} = |\underline{x}_i - \underline{x}_j|$ and a threshold distance d_0 as well as limits for the joint positions $\underline{x}_i$. In that sense equation three of problem (13) must be understood as a component-wise restriction on the joint positions. Fig. 2 sketches the relationship between the joints and their design space. To accommodate joint constraints we modify the linear FE-system by means of a Lagrange multiplier method to include the additional constraint equations.[2] Furthermore, the joints are only allowed to move within the bracket region $\mathbb{B}_B$ and hence the third equation of problem (13) limits the movement of the joints. Finally, there is another restriction to the joint position which prevents an overlap of joints by restricting the distance d_{ij} of two joints to have a minimal distance of d_0.

Incorporating the lacking strength condition (10) is straightforward and yields

$$\begin{aligned} \min_{\varrho_e, \underline{x}_i} \; & c \quad s.t. \quad \underline{\underline{\tilde{K}}}\,\underline{\tilde{u}} - \underline{\tilde{F}} = \underline{0} \\ & 0 \le \varrho_e \le 1 \\ & \underline{x}_{min} \le \underline{x}_i \le \underline{x}_{max} \\ & \frac{\sum_e v_e}{V_0} - v_f \le 0 \\ & \min_{i \neq j} d_{ij} - d_0 \le 0 \\ & \max(LF_p) - 1 \le 0 \end{aligned} \qquad \forall\, e \in \mathbb{B}_B\,,\ \forall\, p \in \mathbb{B}_P \text{ and } \forall i, j = \{1\,,\,\dots\,,\,n_J\}\,. \tag{14}$$

3.4. Simultaneous variation of ply orientations

In addition to the pseudo densities and the joint positions, the angles describing the fiber orientations of the composite laminate plies are also considered as design variables in this section. These variations allow a further adaptation of all involved assembly parts to be optimized. The optimization problem thus becomes

$$\begin{aligned} \min_{\varrho_e, \varphi_i} \; & c \quad s.t. \quad \underline{\underline{K}}\,\underline{u} - \underline{F} = \underline{0} \\ & 0 \le \varrho_e \le 1 \\ & \frac{\sum_e v_e}{V_0} - v_f \le 0 \\ & \max(LF_p) - 1 \le 0 \end{aligned} \qquad \forall\, e \in \mathbb{B}_B\,, \tag{15}$$

which of course can also be extended by the strength condition (10). The variable φ_i can represent either the fiber orientation angle of the entire ply i, uniformly across the panel, or a piecewise definition where each finite element has its own unique fiber orientation. The fiber orientation can also be applied equally to all plies within each element. In this case, all plies in a given element share the same orientation angle φ_i.

3.5. Putting it all together

Eventually, all sub-aspects can be combined into the following compliance optimization problem

$$\begin{aligned} \min_{\varrho_e, \underline{x}_i, \varphi_k} \; & c \quad s.t. \quad \underline{\underline{\tilde{K}}}\,\underline{\tilde{u}} - \underline{\tilde{F}} = \underline{0} \\ & 0 \le \varrho_e \le 1 \\ & \underline{x}_{min} \le \underline{x}_i \le \underline{x}_{max} \\ & \frac{\sum_e v_e}{V_0} - v_f \le 0 \\ & \min_{i \neq j} d_{ij} - d_0 \le 0 \\ & \max(LF_p) - 1 \le 0 \end{aligned} \qquad \forall\, e \in \mathbb{B}_B\,,\ \forall\, k \in \mathbb{B}_P \text{ and } \forall i, j = \{1\,,\,\dots\,,\,n_J\} \tag{16}$$

with the design variables ϱ_e, $\underline{x}_i$ and φ_k, an active volume constraint for the bracket, displacement constraints for the joints and a strength constraint for the panel.

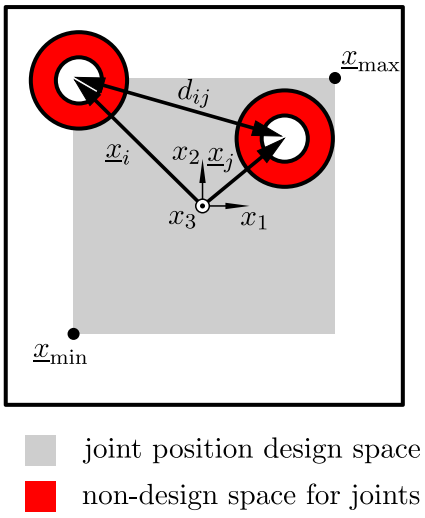

Fig. 2. Schematic sketch of controlling the joint positions via the design variables $\vec{x}_i$.

4. Gradient computation and practical implementation details

The optimization problems from the previous section must be solved using a gradient-based algorithm due to the size of the problem, see [16]. The required gradient computation can become quite involved, since implicit dependencies $\underline{u}_B(\varrho_e, \underline{x}_i, \varphi_i)$ arise from the equality constraint. By means of the adjoint method we can mitigate this problem. An extension to the work of [5] states the incorporation of the strength criterion, which must also be differentiable. In a generic

[2] The displacement constraint of the FE analysis should not be confused with a constraint of the optimization problem.

setting with the generic design variable $\xi \in \{\rho_e, x_i, \varphi_i\}$ we deduce the derivative of the strength condition (10) by means of an adjoint augmentation via

$$\frac{dg_{LF}}{d\xi} = \frac{dg_{LF} + \underline{\lambda}^{\mathrm{T}}\left[\underline{\underline{K}}\,\underline{u} - \underline{F}\right]}{d\xi} = \sum_{g=1}^{n_g} \frac{\partial g_{LF}}{\partial \underline{\sigma}_L}\frac{\partial \underline{\sigma}_L}{\partial \underline{\sigma}_g}\frac{d\underline{\sigma}_g}{d\xi} + \underline{\lambda}^{\mathrm{T}}\left[\frac{d\underline{\underline{K}}}{d\xi}\underline{u} + \underline{\underline{K}}\frac{d\underline{u}}{d\xi}\right] . \tag{17}$$

Here, $\underline{\lambda}$ is the unknown adjoint vector, $\underline{\sigma}_g$ are the stresses in the global coordinate system in Voigt-notation at Gauss point g of the shell elements and $\underline{\sigma}_L$ are the same stresses described in the local shell coordinate system. Due to the aggregative nature of the strength constraint, a summation over all Gauss points n_g must be conducted.[3]

With the matrix $\underline{\underline{B}}_g$ holding the derivatives of the element shape functions and the material matrix $\underline{\underline{C}}_g$ evaluated at Gauss point g we write

$$\underline{\sigma}_g = \underline{\underline{C}}_g\,\underline{\underline{B}}_g\,\underline{u} \tag{18}$$

and eventually get

$$\frac{dg_{LF}}{d\xi} = \underline{\lambda}^{\mathrm{T}}\frac{d\underline{\underline{K}}}{d\xi}\underline{u} + \sum_{g=1}^{n_g}\frac{\partial g_{LF}}{\partial \underline{\sigma}_L}\frac{\partial \underline{\sigma}_L}{\partial \underline{\sigma}_g}\frac{d\underline{\underline{C}}_g}{d\xi}\underline{\underline{B}}_g\,\underline{u} + \left[\sum_{g=1}^{n_g}\frac{\partial g_{LF}}{\partial \underline{\sigma}_L}\frac{\partial \underline{\sigma}_L}{\partial \underline{\sigma}_g}\underline{\underline{C}}_g\,\underline{\underline{B}}_g + \underline{\lambda}^{\mathrm{T}}\underline{\underline{K}}\right]\frac{d\underline{u}}{d\xi} . \tag{19}$$

If we choose the adjoint vector $\underline{\lambda}$ such that the last term vanishes, e.g. solving one linear system of equations (the adjoint system, see for instance [17]), the desired gradients only require the specification of

$$\frac{\partial g_{LF}}{\partial \underline{\sigma}_L} \quad , \quad \frac{\partial \underline{\sigma}_L}{\partial \underline{\sigma}_g} \quad , \quad \frac{d\underline{\underline{K}}}{d\xi} \text{ and } \frac{d\underline{\underline{C}}_g}{d\xi} \quad . \tag{20}$$

The first term in Eq. (20) depends on the failure criterion as detailed in Appendix A.1. The second term in Eq. (20) originates from the transformation from stress tensor coordinates $\underline{\sigma}$ in the global coordinate system to the tensor coordinates $\underline{\sigma}_L$ in the local (shell) coordinate system, i.e.

$$\underline{\sigma}_L = \underline{\underline{T}}\,\underline{\sigma} \qquad \frac{\partial \underline{\sigma}_L}{\partial \underline{\sigma}} = \underline{\underline{T}} \tag{21}$$

with the transformation matrix $\underline{\underline{T}}$. The third term in Eq. (20) represents the derivative of the system matrix and can be computed during the assembly process. The last term in Eq. (20) constitutes the derivative of the material matrix (elasticity tensor in Voigt notation). In the case of ξ being the joint positions, this term vanishes, since joints do not influence the material law on element level. Details concerning the derivative of the system matrix in the presence of joints can be found in [5].

Problems (15) and (16) require the gradients related to the laminate orientations of all layers $\underline{\varphi}$ or of all shell elements φ_i (see last two terms of Eq. (20)). These orientation dependencies emanate from the anisotropic elasticity tensor $\mathbb{C}(\varphi)$ which reads

$$\underline{\underline{C}}_g = \underline{\underline{T}}^{-1}(\varphi)\,\underline{\underline{C}}_g^{\mathrm{Trans}}\,\underline{\underline{T}}^{-\mathrm{T}}(\varphi) \tag{22}$$

in Voigt-notation. Here, $\underline{\underline{C}}_g^{\mathrm{Trans}}$ denotes the material stiffness matrix of the transversal isotropic elasticity tensor in Voigt-notation in the shell coordinate system with the fiber direction aligned along the x-direction. During the assembly process of the global stiffness matrix $\underline{\underline{K}}$, only the panel part $\underline{\underline{K}}_P(\varphi)$ depends on the orientation angles. The computation of the MIT4C element stiffness matrices to assemble the panel part of the global stiffness matrix in Eq. (5) via

$$\underline{\underline{K}}_P = \mathop{\mathrm{A}}_i \underline{\underline{K}}_i^{\mathrm{MIT4C}}(\mathbb{C}(\varphi)) \tag{23}$$

enables the computation of the required derivatives in a straightforward manner. Due to the periodic nature of the orientation angles there are no restricting bounds. However, a practical implementation of the used optimization algorithm requires the formulation of design variable limits. Therefore, we use a generous range of $-6\pi \le \varphi \le 6\pi$. These bounds were never reached during the optimization runs.

Applying Eq. (17) in Problem (11) for the gradient computation is not straightforward, since the max function is non-differentiable. A common way to circumvent this problem is to approximate the max function by an aggregation function e.g. the p-Norm $\|\underline{LF}\|_p = \left[\sum_{j=1}^{p} LF_j^p\right]^{1/p}$, see [18]. This aggregation function is a conservative estimate of the max function, leading to an over-fulfillment of the strength constraint and hence produces a non-optimal structure. Therefore, we follow the suggested heuristic of Le et al. [19] to approximate the max function by introducing a factor c^k, which varies with the optimization iteration k via

$$\max(LF_j) \approx c^k\,\|\underline{LF}\|_p \;\text{ with }\; c^k = \alpha^k\frac{\max(\underline{LF}^{k-1})}{\|\underline{LF}\|_p} + [1-\alpha^k]c^{k-1} \;\text{ and }\; p = 8 . \tag{24}$$

Because c^k tends to oscillate between optimization iterations, the damping factor $\alpha^k \in (0, 1]$ is introduced to minimize these unwanted effects. If α^k decreases, the effects of the previous iteration $k-1$ dominate over the current iteration k, hence leading to smaller changes in c^k. Le et al. [19] do not suggest a general strategy on how to adjust α^k. To that end, we introduce a simple but effective scheme to control the damping parameter, which is shown in Algorithm 1. The algorithm depends on the last two iteration k and $k-1$ to assess a possible oscillatory behavior of c^{k+1}. If an oscillation is detected, α^{k+1} is reduced w.r.t. the current α^k up to a minimum value of 2^{-7}. Otherwise α^{k+1} is increased w.r.t. the current α^k up to a maximum value of one. If the factor c^k converges, the value of the approximation (24) is equal to the value of the max-function. However, due to the change of c^k, the optimization problem slightly changes in every iteration which may impact convergence.

In contrast to the work of [5], we use the globally convergent method of moving asymptotes (GCMMA) [20] to solve all mentioned optimization problems. The GCMMA is an enhanced version of the method of moving asymptotes (MMA) with additional inner iterations to circumvent spurious oscillatory behavior, which we encountered, especially when incorporating the strength constraint. The entire optimization algorithm itself is conducted via four sub-optimization steps in which the projection parameter β from Eq. (8) is successively increased from 1 to 8. The convergence criteria for the sub-optimizations are given by

$$\min\left(\max(\underline{\varrho}_e^k - \underline{\varrho}_e^{k-1}), \|\underline{\varrho}\|_2, \frac{|c^k - c^{k-1}|}{|c^k|}\right) < \epsilon \tag{25}$$

with $\epsilon = 10^{-6}$. If these tight thresholds are not reached, the algorithm stops after 100 iterations to proceed to the next suboptimization. However, due to the highly non-linear strength condition and the iteratively changing optimization problem, the GCMMA does not converge easily. The dominant reason for this cumbersomeness was found in the fact, that the optimization problem changes in every iteration due to the heuristics in (24). Especially during the first iterations, there is typically a substantial adjustment of the c^k factor, which might lead to a severe violation of the strength condition. Therefore, it is not advisable to apply (24) in every iteration. However, it has to be applied at some point to mimic the max-function of the strength condition. Another problem we encountered was the exceedance of the chosen allowed 30 inner iteration within the GCMMA. This means the GCMMA submodel is not conservative enough which in turn leads to oscillating iterates, as it is the case for the pure MMA algorithm. In such cases, the adjustment of c^k is not advisable and would introduce even more cumbersomeness. Eventually, a converged iterate could experience a severe violation of the true max strength criterion (left-hand-side of Eq. (24)). In this context, convergence is qualified by the fulfillment of the volume constraint and the current strength constraint (depending

[3] At this point, we already assumed an aggregated form of the strength condition, as will be discussed later.

Algorithm 1 Algorithm of the update scheme for the parameter c

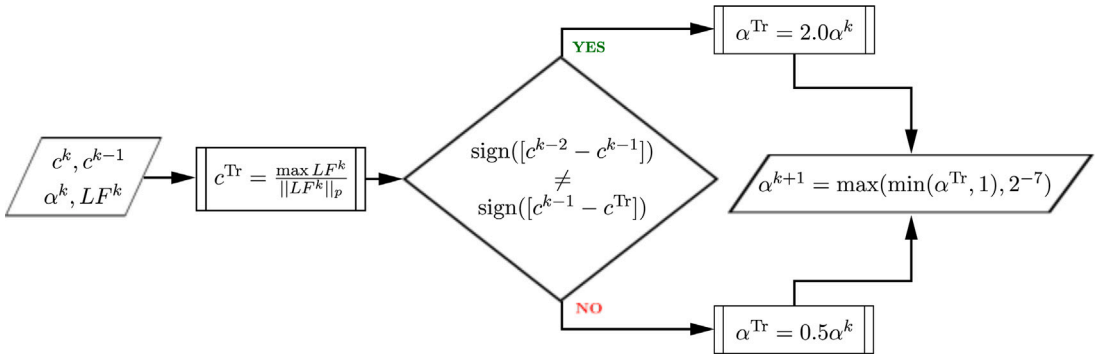

on the current value of c^k). This effect is due to a c^k which is not fully adapted to give an accurate max approximation. Therefore, it is advisable to adjust this factor more often in the course of further iteration steps. To that end, the heuristic (24) is executed if one of the following criteria is met:

- If 10 iterations have passed without executing (24).
- If the inner iterations of the last three outer iterations of the GCMMA did not exceed the maximum allowed iterations of 30.
  - Four outer iterations have passed without executing (24). This allows a proper adjustment of the asymptotes within the GCMMA algorithm which relies on the previous three iterations.
  - If the volume and strength constraints have been fulfilled up to a tolerance of 10^{-4}.

Additionally, the GCMMA parameter that controls the conservativeness is altered as suggested in [21] such that the convex subproblem also approximates the diagonal of the Hessian of the objective function and constraints. Due to the second-order nature, it was found that this enhancement only improves the GCMMA performance at a later, almost converged stage.[4]

A final distinctive feature of the optimization problems involving the strength condition is finding an adequate net force F. Since all deformation analyses depend on this force, it is possible to choose a force large enough such that the strength condition is violated in the entire region of the panel. On the other hand, if F is not large enough, the strength condition might always be fulfilled in the entire panel region. To come up with an optimized design that respects the strength condition, the task is to determine an appropriate force F, such that the strength condition is barely fulfilled in some parts of the panel region. This process requires a manual adjustment procedure and becomes more involved when increasing the complexity of the considered problem.

The Problems and algorithms listed are implemented in an in-house research MATLAB code. This code is designed for rapid development work in the form of object-oriented approaches without focusing on computational speed or numerical efficiency. It is possible to seamlessly change parts of the code such as the optimization algorithm or equation solver. The large degree of freedom in code development in combination with a relatively high number of required iterations necessitates conducting all computations on a high-performance cluster. A significant speedup in computation time is accomplished by precompiling element stiffness routines and the subproblem solver of the GCMMA using MATLAB's MEX-function capabilities. A further improvement is achieved by using an iterative algebraic multigrid solver [22], which was integrated via the MRST-library [23] interface. A typical simulation of Problem (14) with 28 CPUs (3.25 GHz) and 150 GB RAM needs roughly 10 days.

[4] The used parameters of the GCMMA can be provided on request.

5. Results

In this section, we present the results of the formulated optimization problems of the previous section for the example introduced in Section 2. The complexity of the problems gradually increases, which makes convergence more challenging.

Every optimization problem is tested on three different laminate configurations that are defined by the following ply orientations:

1. $[0, 90, 0]$
2. $[0, 0, 0]$
3. $[45, 45, 45]$

While some of these laminates may not be used in practical applications, they effectively illustrate the influence of ply orientations on the bracket design.

5.1. Panel with surface connection

First, we consider the optimization Problems (6) and (11) which are introduced in Section 3.2. Table 2 shows the contour plots of the solution for the topology optimization together with the load factor in the laminate. In the following, the largest load factor through the thickness is always shown.

The first row of Table 2 shows the results of the plain topology optimizations without an active strength constraint. For the first two laminates, the optimizer tends to place material along the edges of the bracket's design space to reduce bending moments in the panel by minimizing the lever arm from the bracket-panel connection to the clamped boundary of the panel. Because the fibers are primarily oriented along the x_1-direction, the evolved stiffening bars align with this axis to effectively increase bending resistance. Since the $[0, 0, 0]$ laminate lacks reinforcement in the 90° direction, additional stiffening bars extend from the bracket edges toward the panel center. For the third laminate ($[45, 45, 45]$), a distinct pattern emerges, showing gaps oriented along the reinforced 45° fiber direction, which enhances bending resistance around this axis. Additionally, every structure shows symmetries that are correlated to the underlying panel reinforcements.

Due to the absence of the strength criterion, the load factor is visibly exceeded for all three variants in some regions. Magenta regions in the load factor contour plots indicate these violations, mainly concentrated at the bracket corners for the first two laminates, due to complex stress states within these locations. Interestingly, failure occurs at the corners of the panel for example three. Due to the $[45, 45, 45]$ laminate fiber orientations, the failure onset of the panels is shifted from the

Table 2
Comparison of assembly optimization without and with strength constraint for different fiber layups.

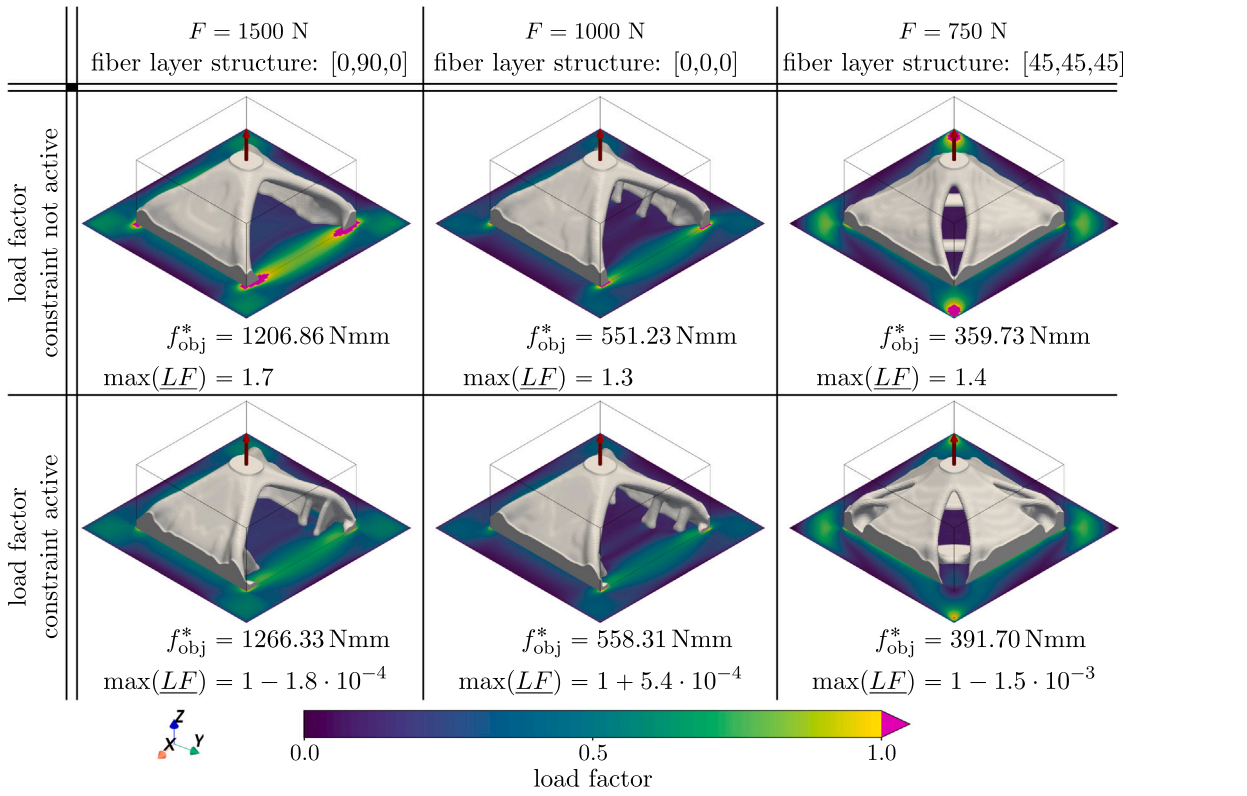

bracket design space boundary to these corners. The magnitudes of these violations are significant, ranging from a 37% to a 66% overshoot.

If we activate the strength constraint, these violations vanish and only isolated elements show load factors larger than 1. However, these overshoots are on the order of 10^{-4} and may be regarded as numerical artifacts. These isolated elements occur at the same regions as the failure regions in the optimizations without strength constraint. Examining the bracket topology reveals that additional stiffened fillets and bars are formed to mitigate high stress gradients and hence failure in the panel. For the third laminate, more gaps form to allow broader stiffening structures with the limited amount of material available. These modifications increase the compliance by approximately 2% to 5%.

The convergence behavior can be studied by inspecting Fig. 3, which shows the evolution of the objective function as well as the evolution of the volume constraint.

Constraints are shown in a symmetric logarithmic scale, see [24], to emphasize convergence details. The convergence is fourfold due to the successively increased projection parameter β, which is indicated by different color shading. Initially, significant reductions in the objective function occur as the algorithm identifies the optimized topology in a gross manner. After increasing β, a small jump in the constraints and objective function is observable. These discontinuities are due to a change of the optimization problem. The utilization of the GCMMA prevents oscillations to a great extent.

Fig. 4 exemplarily shows the convergence behavior of the same example but with activated strength constraint. This time, the constraint plot is extended by the evolution of the strength constraint (24). While the course of the objective function over the iterations does not differ very much from the one in Fig. 3, there are much larger fluctuations visible for the constraints. Due to the heuristic damping Algorithm 1, convergence becomes more complex. At the beginning of the optimization, both constraints are violated significantly on the order of magnitude of one. However, only a few iterations are needed to satisfy both constraints. Then, after the first 10 iterations, the adaptation heuristic of Algorithm 1 applies. This again entails a severe violation of the strength constraint, which is mitigated by subsequent iterations until the heuristic applies again. The process continues until both constraints are converging to an order of magnitude smaller than 10^{-4} at approximately iteration 60. Then, the heuristic applies more frequently (almost every four iterations) leading to characteristic overshooting peaks of the strength constraint, which are typically mitigated within one subsequent iteration. When transitioning from one suboptimization to another, while increasing β, significant changes of the constraints are visible. Hence, more iterations are needed for the constraints to converge again. Larger β-values require more iterations to reach a convergence region of violations on the order of 10^{-4}. This is due to the increasingly more non-linear character of the projection (8) resulting in steeper gradients.

Since the optimization algorithm utilizes an approximation of the maximum-function of the load factor, it is instructive to inspect the course of convergence of the true maximum load factor, as shown in Fig. 5, together with the approximation of the (differentiable) p-norm. Early iterations show oscillations in the true maximum of the load factor due to shifting failure hotspot locations, which the p-norm smooths out, albeit with a conservative overestimation roughly by a factor of about two. Significant changes of the topology in that phase entail significant changes of maximum stress locations on the panel. This effect leads to a steadily changing position of the element associated with that maximum load factor. The p-norm mitigates this phenomenon. However, as can be seen, the p-norm overestimates the maximum-function by a factor of two and hence conservatively restricts the optimization potential.

Fig. 5 also depicts the evolution of the damping parameter α^k and factor c^k. Initial oscillations in c^k trigger reductions in α^k to stabilize the

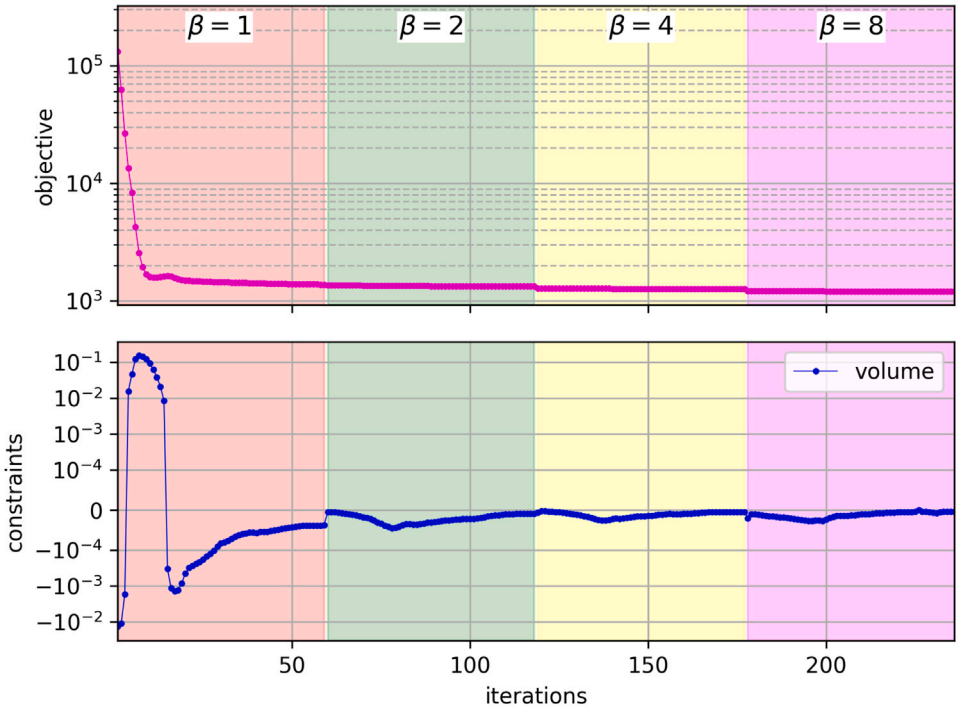

Fig. 3. Course of convergence of the objective function and constraint for example 1 with a [0,90,0] laminate panel and no strength constraint activated.

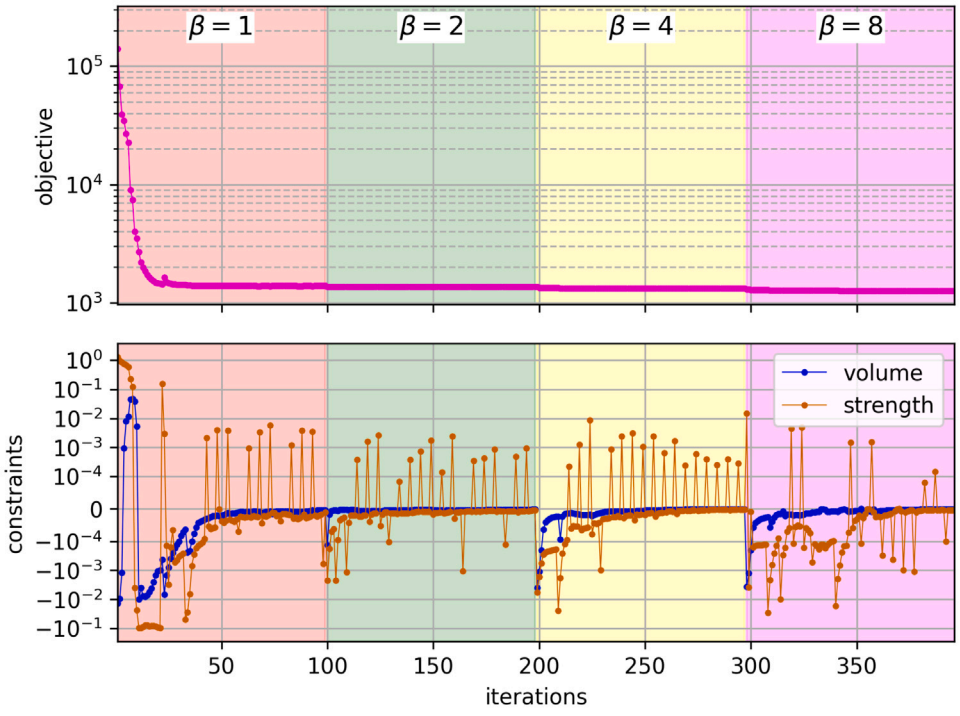

Fig. 4. Course of convergence of the objective function and constraints for example 1 with a [0,90,0] laminate panel and activated strength constraint.

optimization. A reduction by a factor of two secures a smooth optimization immediately. Consequently, α^k increases to the desired value of one within the next iteration. Then, changes of c^k are more severe again and hence increase the impact on the strength constraint. Oscillations of c^k start again and the cycle repeats. These cycles of damping and recovery persist throughout the entire optimization process. During the shift from suboptimization with $\beta = 1$ to $\beta = 2$ three reductions of α^k are required for stabilization. It can be noted that the smallest α^k reached has a value of 0.0625, which is quite reasonable. These relatively high values result in a converging c^k and hence attest a good

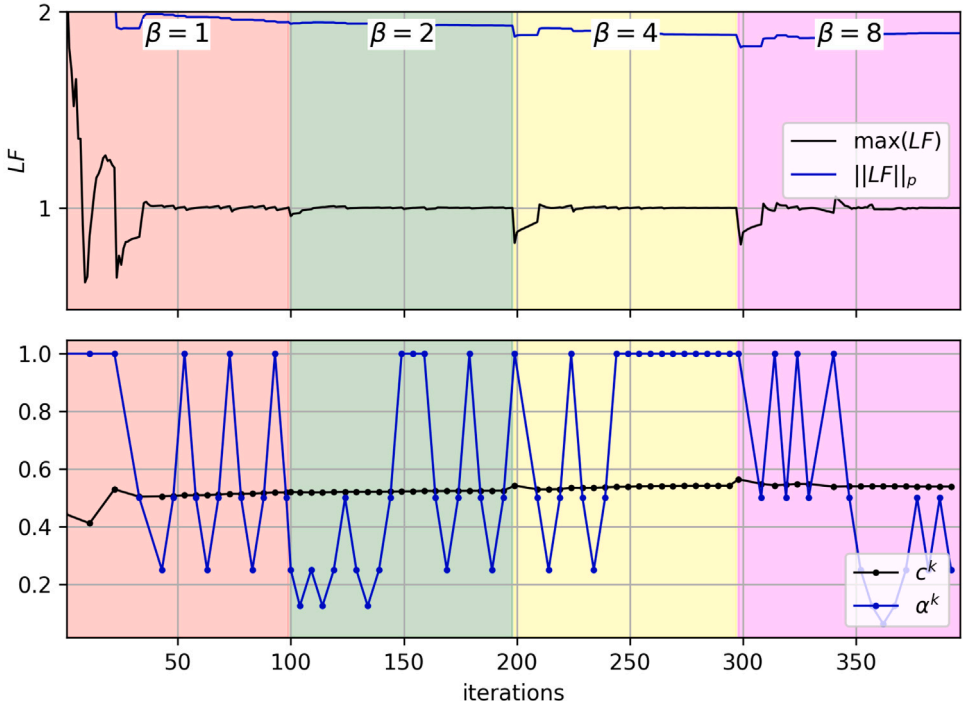

Fig. 5. Course of convergence of the p-Norm and maximum norm of the load factor of example 1 with a [0,90,0] laminate panel and activated strength constraint as well as the course of the c^k factor and the damping parameter α^k of the heuristic (24).

approximation of the maximum-function. Therefore, although $\alpha^k \neq 1$ at the last iteration, the course of c^k is sufficient for the fulfillment of the strength constraint up to a numerical acceptable error.

5.2. Panel connected by joints

Table 3 presents the optimized structures obtained by solving Problems (13) and (14), where the bracket is connected to the panel via four discrete joints. The initial joint positions, as shown in Fig. 1, are symmetrically distributed in the centers of the four quadrants of the x_1–x_2-plane (panel plane) such that

$$\underline{x}_1^{\text{init}} = \begin{bmatrix} 5 \\ 5 \end{bmatrix}, \quad \underline{x}_2^{\text{init}} = \begin{bmatrix} -5 \\ 5 \end{bmatrix}, \quad \underline{x}_3^{\text{init}} = \begin{bmatrix} 5 \\ -5 \end{bmatrix} \quad \text{and} \quad \underline{x}_4^{\text{init}} = \begin{bmatrix} -5 \\ -5 \end{bmatrix}. \tag{26}$$

In all cases, the joints position themselves near the corners of the bracket design space, maximizing the distance from the load application location. Hence, the load factor constraint and fiber layer structure do not have any effect on the optimal joint position. The optimal joint positions are solely dominated by increasing the overall stiffness of the assembly by reducing the bending moments in the panel. Compared to the surface-connected models in the previous section, the net forces applied in the joint-connected cases are significantly lower. The choice of these forces is primarily dictated by the simulations with active strength constraints. Because the joints transfer loads through ring-shaped contact areas, stress concentrations arise around these locations, often leading to failure, especially in examples 1 and 2. These localized failures necessitate substantially reduced load levels to ensure that feasible solutions exist, that satisfy the strength constraints. Fig. 6 illustrates the failure zone around one joint for example 2 with deactivated strength constraint. To visualize the stress concentration induced failure near the joints, a detailed view of one joint without the optimized bracket is shown in a magnified way.

Looking at the first row of Table 3, we observe, that the strength constraint is violated for all examples. In contrast to examples 1 and 2, the $[45, 45, 45]$ laminate fails primarily at the panel corners aligned with its principal reinforcement direction, rather than near the joints. However, these violations are not as severe as those observed in the corresponding unconstrained surface-connected examples, see Table 2. When the strength constraint is active, the heuristic (24) successfully enforces the constraint to a tight numerical tolerance on the order of 10^{-4} or lower. The topology of example 1 remains largely unchanged when the strength constraint is active. In contrast, example 2 and especially example 3 exhibit notable modifications. For the $[45, 45, 45]$ laminate a distinctive bridge-like structure forms in the $-45°$ direction, enhancing the bending resistance transverse to the ply orientation.

Fig. 7 depicts the convergence history of example 3 with active strength constraint. The additional complexity introduced by movable joints results in a more erratic constraint behavior during iteration. Substantial changes to topology and joint positions primarily occur up to the third sub-optimization step ($\beta = 4$), after approximately 250 iterations. The subsequent iterations result in incremental improvements only. These findings highlight again the increased difficulty of the simultaneous topology and joint position optimization.

Despite the volatile course of the constraints over iteration, as shown in Fig. 8, the true maximum load factor decreases rapidly within 50 iterations to the target value of one.

For completeness, Fig. 8 also shows the evolution of the heuristic factor c^k and the damping factor α^k (see. Eq. (24)). c^k constantly oscillates through the course of convergence. However, these oscillations are not too severe which can be seen by the damping factor alternating between 1 and 0.125 in a regular fashion, ultimately leading to a very good satisfaction of the strength condition.

5.3. Ply orientation optimization

As a final variation of the considered problems, the ply orientation angles are allowed to vary, leading to the formulation given in Problems (15) and (16). This modification permits adjustments of the panel's structural parameters. Table 4 presents the results for three possible optimization variants. The first column shows the orientation optimization of the three plies, where the orientation angles in the x_1–x_2-plane are uniform across the panel for every ply. This variant

Table 3
Comparison of assembly optimization with four joints without and with strength constraint activated for different fiber layups.

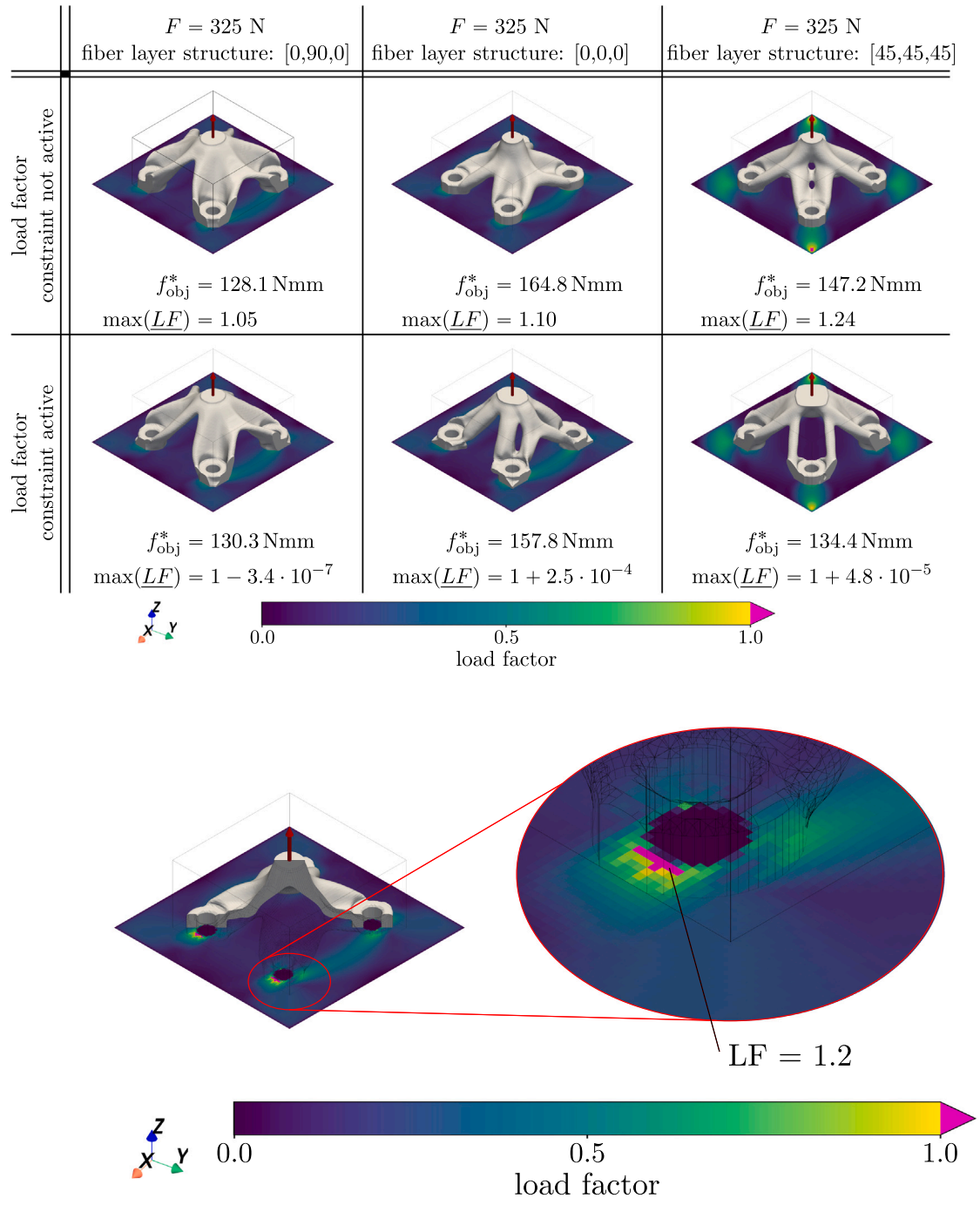

Fig. 6. Detailed contour plot of the load factor of the optimized assembly of example 2 with a $[0, 0, 0]$ laminate panel and connecting joints. Failure regions are visible due to the detailed panel display of one joint connection without the optimized bracket.

aligns well with practical manufacturing processes where the ply angle can be controlled uniformly during lamination. The second and third columns present results from an element wise variable laminate orientation. Here, for every individual element all ply orientations are aligned, but can change from element to element. Such highly localized variations pose significant challenges for the manufacturing process. Incorporating manufacturing constraints such as orientation smoothing via filtering and path-planning, as discussed in [6,25], would be necessary to obtain manufacturable designs; however, these are beyond the scope of the present study. Orientation optimization is very sensitive to the initial orientation angles. To that end we do not consider random initialization of the orientation angles but instead utilize a predefined laminate layup of $[0, 0, 0]$.

Inspection of the optimized topologies reveals that variant (a) produces a design similar to those presented in Section 5.1. Interestingly, two plies align, while the third deviates, producing an effective layup similar to a $[0, 90, 0]$ laminate. Fig. 9 shows the evolution of these ply angles over the course of convergence. In the beginning of the optimization, the angles do not change too much whereas the topology does. After approximately 60 iterations, the gross of the topology has

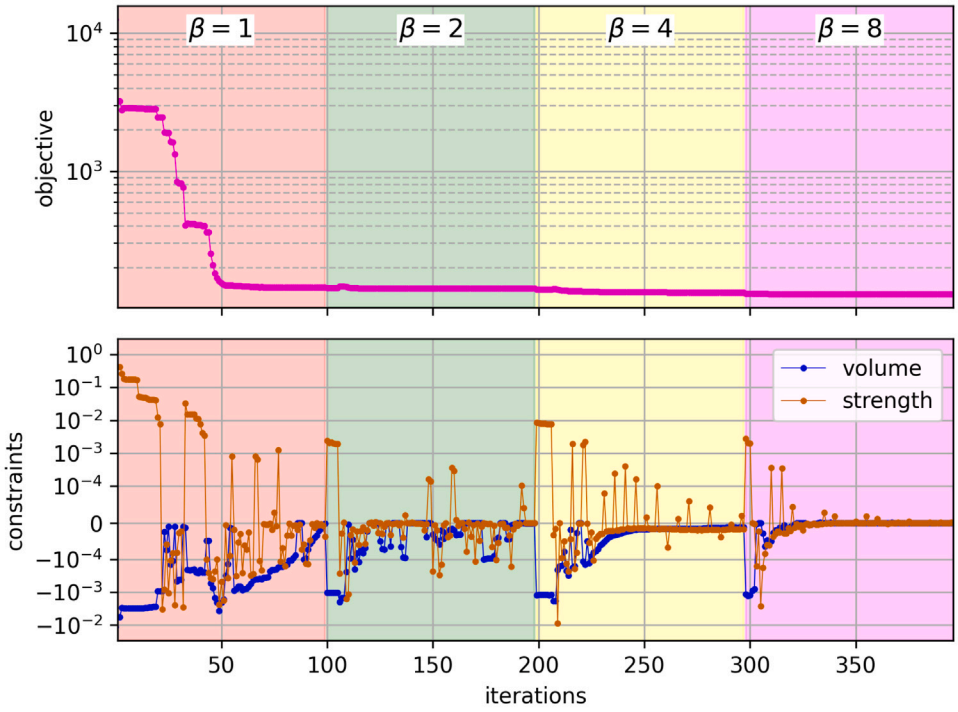

Fig. 7. Course of convergence of the objective function and constraints for example 3 with a [45,45,45] laminate panel, connecting joints and activated strength constraint.

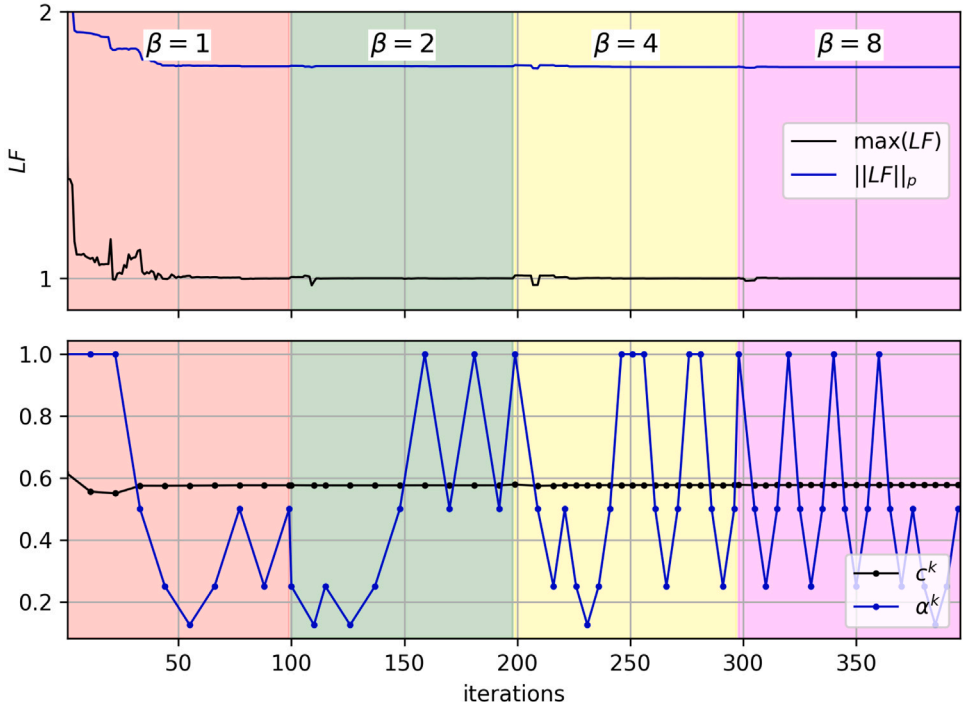

Fig. 8. Course of convergence of the p-Norm and maximum norm of the load factor of example 3 with a [45,45,45] laminate panel, connecting joints and activated strength constraint as well as the course of the c^k factor and the damping parameter α^k of the heuristic (24).

formed and the change of ply angles contributes more to the compliance. At approximately 270 iterations, the ply angles seem to converge eventually.

Variant (b) yields a topology that differs significantly from those observed in Section 5.1. Due to the variable orientation field, a double symmetric bracket structure evolves. The optimized orientation field

Table 4
Comparison of assembly optimizations with strength constraint and variable ply orientations: (a) uniformly variable ply orientation across the panel, (b) locally variable ply orientations and (c) locally variable ply orientations with connecting joints.

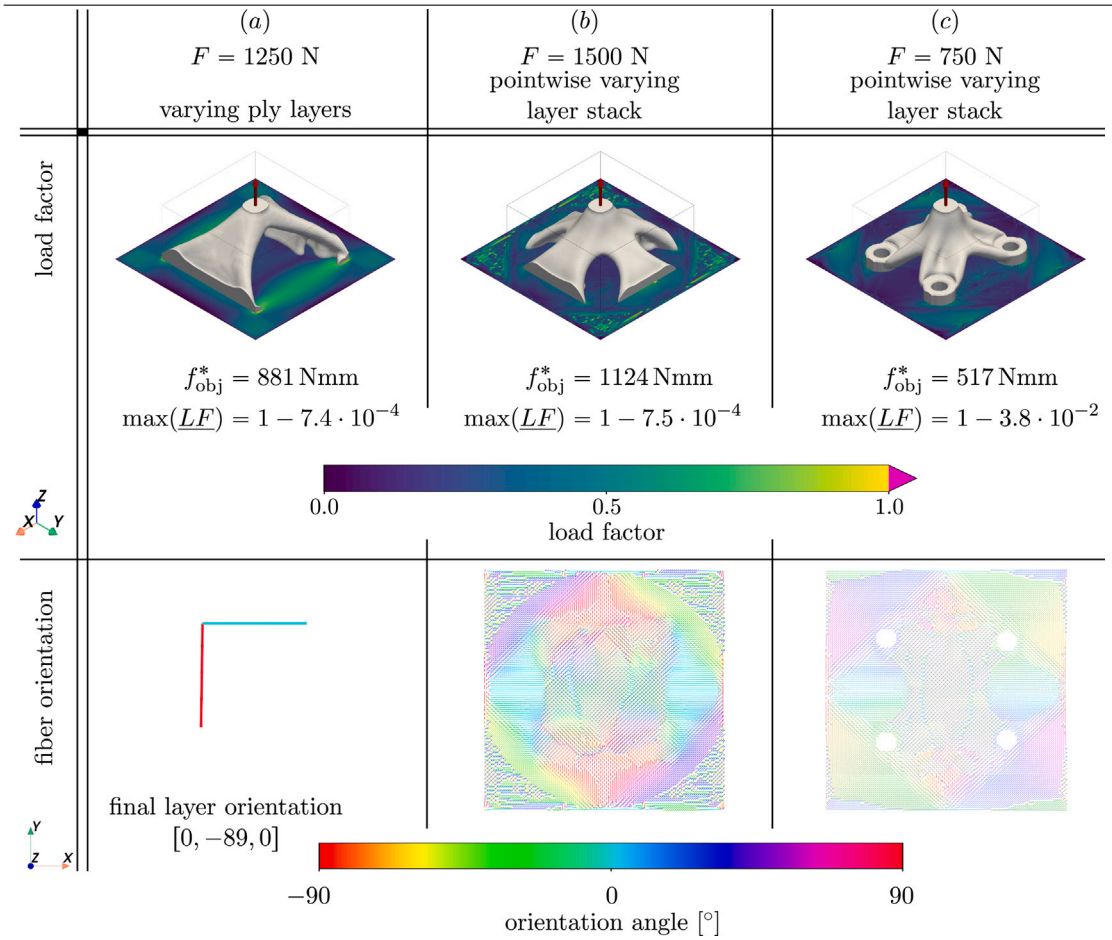

exhibits a circular pattern surrounding the bracket, with fiber directions aligning closely with the principal directions of force transmission. In regions such as the panel corners, where bracket material is absent, the fiber orientations display a more diffuse or less structured distribution.

Variant (c) yields a topology quite similar to those observed in Section 5.2. The bolt positions shift toward the boundaries of the bracket design space. The optimized orientation field again aligns with the directions of force transmission. However, the fulfillment of the Tsai–Wu-criterion is not as precise anymore, which results from the highly demanding optimization problem.

6. Conclusion

This paper extends the work of [5] on simultaneous topology optimization of assemblies, demonstrated using an isotropic metallic bracket mounted on a composite laminate panel with three unidirectional fiber-reinforced plies. The connection between the panel and bracket is modeled either as a continuous surface bond or through a discrete set of joints. By incorporating strength constraints based on the Tsai–Wu failure criterion, the approach enables the holistic optimization of assemblies that ensure both stiffness and structural integrity requirements. Results of the benchmark example demonstrate that the inclusion of such constraints, as well as accounting for fiber orientation variations, substantially affects the optimal topology.

Our results reveal significant differences between designs obtained with and without strength considerations, as well as between surface-connected and joint-connected assemblies. The simultaneous variation of ply orientations further enriches the design space, yielding non-trivial optimized fiber layouts aligned with force transmission paths. These findings underscore the critical importance of considering the entire assembly — encompassing topology, joint locations, and laminate orientations — in a unified optimization process to fully exploit the potential for lightweight yet robust structural solutions.

Nevertheless, the simultaneous optimization of multiple design domains and constraints introduces considerable numerical and algorithmic challenges. The problem complexity necessitates careful tuning of hyperparameters, robust treatment of nonlinear and non-differentiable constraints and the use of advanced optimization algorithms. Moreover, selecting appropriate load cases to activate strength constraints without inducing unbounded failure proved challenging. These challenges highlight the need for ongoing research on efficient solution strategies and automated parameter selection to facilitate a practical application in industrial design workflows.

In conclusion, the proposed simultaneous optimization framework advances the state of the art in coupled metal-composite assemblies and provides a foundation for future research into manufacturable constraints, multi-load scenario analyses, and experimental validation.

CRediT authorship contribution statement

Konrad Schneider: Writing – original draft, Visualization, Validation, Software, Methodology, Investigation. **Olaf Ambrozkiewicz:** Writing – review & editing, Software, Methodology, Formal analysis, Conceptualization. **Benedikt Kriegesmann:** Writing – review &

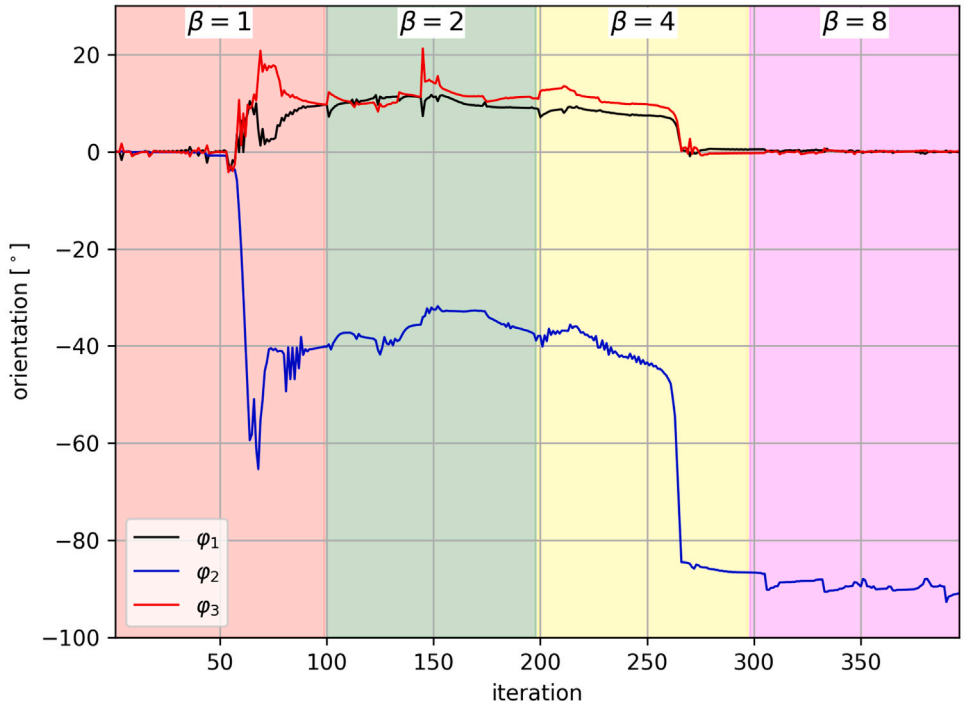

Fig. 9. Evolution of the ply orientations for the variation with a net force of $F = 1250$.

editing, Supervision, Methodology, Investigation, Funding acquisition, Conceptualization.

Declaration of competing interest

The authors declare the following financial interests/personal relationships which may be considered as potential competing interests: Benedikt Kriegesmann reports financial support was provided by German Research Foundation. If there are other authors, they declare that they have no known competing financial interests or personal relationships that could have appeared to influence the work reported in this paper.

Acknowledgments

This research was funded by the German Research Foundation (DFG) via project No. 406315228. The statements in this contribution do not necessarily represent the opinion of the DFG.

Appendix

A.1. Derivatives of the load factor based on the Tsai–Wu failure criterion

The Tsai–Wu-criterion itself is quadratic w.r.t. the stress $\boldsymbol{\sigma}_L$ in the local coordinate system. In a computational setting we collect the stress tensor coordinates via the well-known Voigt-notation in a vector $\underline{\sigma}_L = [\sigma_{x'x'}\ ,\ \sigma_{y'y'}\ ,\ \sigma_{x'y'}]^T$. The reserve factor RF is introduced such that it linearly scales the stress to the reserve stress

$$\underline{\sigma}_{RF} = RF\underline{\sigma}_L$$

which is used in the Tsai–Wu-criterion. The Tsai–Wu-criterion itself then becomes

$$F(\underline{\sigma}_{RF}) = F(RF\underline{\sigma}_L) = RF\underline{\sigma}_L^T\underline{F} + RF^2\underline{\sigma}_L^T\underline{\underline{F}}\,\underline{\sigma}_L \le 1 \tag{27}$$

with the Tsai–Wu coefficient vector $\underline{F}$ and coefficient matrix $\underline{\underline{F}}$. For the onset of failure, when reaching a failure stress $\underline{\sigma}_L \to \underline{\sigma}_L^*$, we have $F(\underline{\sigma}_{RF}^*) = 1$ which gives

$$RF = \frac{-R_1 + \sqrt{R_1^2 + 4R_2^2}}{2R_2} \quad \text{with} \quad R_1 = \underline{\sigma}_L^{*\,T}\underline{F} \quad \text{and} \quad R_2 = \underline{\sigma}_L^{*\,T}\underline{\underline{F}}\,\underline{\sigma}_L^* \,. \tag{28}$$

Due to stability reasons the Tsai–Wu coefficients must fulfill $\underline{\underline{F}} \succ 0$. For the optimization, RF is disadvantageous since for $|\underline{\sigma}_L| \to \underline{0}$ we have $RF \to \infty$ which might lead to numerical instabilities. A remedy is to consider the altered load factor

$$LF = \frac{1}{RF} = \frac{2R_2}{-R_1 + \sqrt{R_1^2 + 4R_2 + \epsilon^2}}\,, \tag{29}$$

which is the inverse of the reserve factor. For numerical stability reasons $\epsilon = 10^{-14}$ is added to the denominator to prevent division by zero. This formulation guarantees

$$\begin{aligned} |\underline{\sigma}_L| \to 0 \ &\Rightarrow\ LF \to 0 \\ |\underline{\sigma}_L| \to \infty \ &\Rightarrow\ LF \to \infty \\ \underline{\sigma}_L \to \underline{\sigma}_L^* \ &\Rightarrow\ LF \to 1 \end{aligned} \tag{30}$$

such that the optimization constraint eventually becomes numerically benign with

$$g(\underline{\sigma}_L) = LF(\underline{\sigma}_L) - 1 \le 0 \tag{31}$$

of which we require the gradient. Using the chain rule we note the gradient as

$$\begin{aligned} \frac{\partial g}{\partial \underline{\sigma}_L} = \frac{\partial LF}{\partial \underline{\sigma}_L} &= \frac{\partial LF}{\partial RF}\frac{\partial RF}{\partial \underline{\sigma}_L} = -\frac{1}{RF^2}\left[\frac{\partial RF}{\partial R_1}\frac{\partial R_1}{\partial \underline{\sigma}_L} + \frac{\partial RF}{\partial R_2}\frac{\partial R_2}{\partial \underline{\sigma}_L}\right] \\ &= -\frac{1}{RF^2}\left[\frac{\frac{R_1}{\sqrt{R_1^2+4R_2^2}} - 1}{2R_2}\underline{F} + \frac{R_1\left[\sqrt{R_1^2+4+R_2^2} - R_1\right]}{2R_2^2\sqrt{R_1^2+4+R_2^2}}2\underline{\underline{F}}\,\underline{\sigma}_L\right]. \end{aligned} \tag{32}$$

Data availability

No data was used for the research described in the article.

References

[1] Nguyen AT, Brandt M, Feih S, Orifici AC. Pin pull-out behaviour for hybrid metal-composite joints with integrated reinforcements. Compos Struct 2016;155:160–72. http://dx.doi.org/10.1016/j.compstruct.2016.07.047, URL https://www.sciencedirect.com/science/article/pii/S0263822316312648.

[2] Kranz J. Methodik und Richtlinien für die Konstruktion von laseradditiv gefertigten Leichtbaustrukturen. Springer Berlin Heidelberg; 2017, http://dx.doi.org/10.1007/978-3-662-55339-8.

[3] Emmelmann C, Herzog D, Kranz J. 10 - design for laser additive manufacturing. In: Brandt M, editor. Laser additive manufacturing. Woodhead publishing series in electronic and optical materials, Woodhead Publishing; 2017, p. 259–79. http://dx.doi.org/10.1016/B978-0-08-100433-3.00010-5, URL https://www.sciencedirect.com/science/article/pii/B9780081004333000105.

[4] Fiorentin F, Oliveira B, Pereira J, Correia J, de Jesus AM, Berto F. Fatigue behavior of metallic components obtained by topology optimization for additive manufacturing. Frat Integrità Strutt 2020;15(55):119–35. http://dx.doi.org/10.3221/igf-esis.55.09.

[5] Ambrozkiewicz O, Kriegesmann B. Simultaneous topology and fastener layout optimization of assemblies considering joint failure. Internat J Numer Methods Engrg 2021;122(1):294–319. http://dx.doi.org/10.1002/nme.6538, URL https://onlinelibrary.wiley.com/doi/abs/10.1002/nme.6538.

[6] Dong Y, Ye H, Xiao Y, Li J, Wang W. Topology optimization method for light-weight design of three-dimensional continuous fiber-reinforced polymers (CFRPs) structures. Compos Struct 2025;354:118819. http://dx.doi.org/10.1016/j.compstruct.2024.118819.

[7] Montemurro M, Mas A, Zerrouq S-e. Topology and anisotropy optimisation of continua using non-uniform rational basis spline entities. Comput Methods Appl Mech Engrg 2024;420:116714. http://dx.doi.org/10.1016/j.cma.2023.116714.

[8] Steltner K, Kipping J, Schüppstuhl T, Kriegesmann B. A workflow for designing stiffness-optimized structures in the context of additive manufacturing of endless fiber-reinforced composites. J Thermoplast Compos Mater 2025;38(8):3116–45. http://dx.doi.org/10.1177/08927057251332788.

[9] Ashby MF, Shercliff H, Cebon D. Materials. Elsevier LTD, Oxford; 2013, URL https://www.ebook.de/de/product/20583789/michael_f_ashby_hugh_shercliff_david_cebon_materials.html.

[10] Camanho P, Maimí P, Dávila C. Prediction of size effects in notched laminates using continuum damage mechanics. Compos Sci Technol 2007;67(13):2715–27. http://dx.doi.org/10.1016/j.compscitech.2007.02.005.

[11] Tsai SW, Wu EM. A general theory of strength for anisotropic materials. J Compos Mater 1971;5(1):58–80. http://dx.doi.org/10.1177/002199837100500106.

[12] Dvorkin EN, Bathe K-J. A continuum mechanics based four-node shell element for general non-linear analysis. Eng Comput 1984;1(1):77–88. http://dx.doi.org/10.1108/eb023562.

[13] Ko Y, Lee P-S, Bathe K-J. A new MITC4+ shell element. Comput Struct 2017;182:404–18. http://dx.doi.org/10.1016/j.compstruc.2016.11.004.

[14] Montemurro M. On the structural stiffness maximisation of anisotropic continua under inhomogeneous Neumann–Dirichlet boundary conditions. Compos Struct 2022;287:115289. http://dx.doi.org/10.1016/j.compstruct.2022.115289.

[15] Bendsøe MP. Optimal shape design as a material distribution problem. Struct Optim 1989;1(4):193–202. http://dx.doi.org/10.1007/bf01650949.

[16] Sigmund O. On the usefulness of non-gradient approaches in topology optimization. Struct Multidiscip Optim 2011;43(5):589–96. http://dx.doi.org/10.1007/s00158-011-0638-7.

[17] Holmberg E, Torstenfelt B, Klarbring A. Stress constrained topology optimization. Struct Multidiscip Optim 2013;48:33–47.

[18] Lund E. Discrete material and thickness optimization of laminated composite structures including failure criteria. Struct Multidiscip Optim 2017;1–19. http://dx.doi.org/10.1007/s00158-017-1866-2, URL https://link.springer.com/article/10.1007/s00158-017-1866-2.

[19] Le C, Norato J, Bruns T, Ha C, Tortorelli D. Stress-based topology optimization for continua. Struct Multidiscip Optim 2009;41(4):605–20. http://dx.doi.org/10.1007/s00158-009-0440-y.

[20] Svanberg K. A class of globally convergent optimization methods based on conservative convex separable approximations. SIAM J Optim 2002;12(2):555–73. http://dx.doi.org/10.1137/S1052623499362822.

[21] Bruyneel M, Duysinx P. Note on topology optimization of continuum structures including self-weight. Struct Multidiscip Optim 2004;29(4):245–56. http://dx.doi.org/10.1007/s00158-004-0484-y.

[22] Demidov D. AMGCL —A C++ library for efficient solution of large sparse linear systems. Softw Impacts 2020;6:100037. http://dx.doi.org/10.1016/j.simpa.2020.100037.

[23] Lie K-A. An Introduction to Reservoir Simulation Using MATLAB/GNU Octave: User Guide for the MATLAB Reservoir Simulation Toolbox (MRST). Cambridge University Press; 2019, http://dx.doi.org/10.1017/9781108591416.

[24] Webber JBW. A bi-symmetric log transformation for wide-range data. Meas Sci Technol 2012;24(2):027001. http://dx.doi.org/10.1088/0957-0233/24/2/027001.

[25] Jantos DR, Hackl K, Junker P. Topology optimization with anisotropic materials, including a filter to smooth fiber pathways. Struct Multidiscip Optim 2020;61(5):2135–54. http://dx.doi.org/10.1007/s00158-019-02461-x.